H3K9 methylation enhances HP1-associated epigenetic silencing complex assembly and suppresses off-chromatin binding

Ziyuan Chen[1], Melissa Seman[2], Ali Farhat[3], Yekaterina Fyodorova[4], Saikat Biswas[5], Alexander Levashkevich[2], Peter L. Freddolino[3,5], Julie S. Biteen[1,4]*, Kaushik Ragunathan[2]*

AFFILIATIONS

[1] Department of Biophysics, University of Michigan, Ann Arbor, MI 48109 USA.

[2] Department of Biology, Brandeis University, Waltham, MA 02451 USA.

[3] Department of Computational Medicine and Bioinformatics, University of Michigan Medical School, Ann Arbor, MI 48109 USA.

[4] Department of Chemistry, University of Michigan, Ann Arbor, MI 48109 USA.

[5] Department of Biological Chemistry, University of Michigan Medical School, Ann Arbor, MI 48109 USA.

*To whom correspondence should be addressed: kaushikr@brandeis.edu, jsbiteen@umich.edu

ABSTRACT

Histone H3 lysine 9 methylation (H3K9me) epigenetically silences gene expression by forming heterochromatin. Proteins called HP1, which contain specialized reader domains, bind to H3K9me and recruit factors that regulate epigenetic silencing. Though these interactions have been identified *in vitro*, we do not understand how HP1 proteins specifically and selectively bind to heterochromatin-associated factors within the nucleus. Using fission yeast as a model system, we measured the single-molecule dynamics associated with two archetypal HP1 paralogs, Swi6 and Chp2, and inferred how they form complexes with their interacting partners: Epe1, a putative H3K9 demethylase; Clr3, a histone deacetylase; and Mit1, a chromatin

remodeler. Through a series of genetic perturbations that affect H3K9 methylation and HP1-mediated recruitment, we were able to track altered diffusive properties associated with each HP1 protein and its binding partner. Our findings show that the HP1-interacting proteins we investigated only co-localize with Swi6 and Chp2 at sites of H3K9me. When H3K9me is absent, Epe1 and Swi6 exhibit diffusive states consistent with off-chromatin interactions. Our results suggest that histone modifications like H3K9 methylation are not simply inert binding platforms but rather, they can shift the balance of HP1 complex assembly toward a predominantly chromatin-bound state. By inferring protein-protein interactions based on the altered mobilities of proteins in living cells, we propose that H3K9 methylation can stimulate the assembly of diverse HP1-associated complexes on chromatin.

SIGNIFICANCE STATEMENT

During differentiation, epigenetic silencing is essential for preserving cellular identity. Establishing and maintaining epigenetic silencing depends on histone H3 lysine 9 methylation, which HP1 proteins recognize and bind with low micromolar affinity and millisecond-scale kinetics. HP1 proteins also recruit diverse histone modifiers to maintain gene silencing. HP1 protein biochemistry has revealed what ***can*** happen, but the state-of-the-art in this field includes little about what ***does*** happen in the complex and crowded environment of the nucleus. Using single-molecule tracking of HP1 proteins and their binding partners, we identified the rules that govern their complex formation in the native chromatin context, and we found that chromatin—previously thought to be an inert platform—enhances complex formation between HP1 and its binding partners.

INTRODUCTION

Genetically identical cells can exhibit different phenotypic characteristics due to the covalent modification of DNA packaging proteins called histones (1). One modification, histone H3 lysine 9 methylation (H3K9me), is enriched within non-transcribed regions of the genome, called heterochromatin (2). Heterochromatin is important for maintaining the integrity of the genome, silencing repetitive DNA sequences, and maintaining cell identity (3). The function of epigenetic modifications like H3K9 methylation relies on the actions of specific proteins called histone modifiers. These include "writer" proteins that add modifications to histones, "reader" proteins that recognize and bind to these modifications, and "eraser" proteins that remove these modifications (1). Histone modifiers often form large multi-protein complexes with other accessory factors to regulate chromatin structure, genome organization, and transcription (3, 4).

H3K9 methylation acts as a binding platform for the recruitment of a conserved family of proteins called HP1 (2). HP1 proteins play multiple roles in forming heterochromatin (5, 6). This includes the recruitment of histone modifiers that catalyze H3K9 methylation deposition and spreading across large chromosomal regions, chromatin compaction through oligomerization, and epigenetic inheritance after DNA replication (7). HP1 proteins recognize H3K9 methylation through a conserved domain called the chromodomain (CD) and interact with their binding partners through a second protein domain called the chromoshadow domain (CSD) (5, 6). Our current understanding is that H3K9 methylated chromatin simply acts as a scaffold that recruits HP1 and its partner proteins to silence transcription (8).

In the model organism *Schizosaccharomyces pombe (S. pombe*), H3K9 methylation is enriched at the pericentromeric repeats, telomeres, and the mating type locus. The protein Clr4 is responsible for adding methyl groups to histone H3 lysine 9 (H3K9me), to create a binding site for HP1 proteins (9). Two HP1 orthologs bind to H3K9me in *S. pombe*: Swi6 and Chp2 (10–12). Despite their structural similarity and shared evolutionary origin, Swi6 and Chp2 are expressed at very different levels in the cell and have distinct roles in heterochromatin formation

(13). Swi6 is expressed at levels that are at least 100 times higher than Chp2 in cells (14). *In vitro* studies of Swi6 and Chp2 capture key biochemical features associated with oligomerization and their interaction with mononucleosomes and oligonucleosomes (7, 14, 15). Such studies have shown that Swi6 and Chp2 have similar tendencies to form dimers and oligomers (16), but Swi6 binds more strongly to nucleosomes (approximately 3-fold higher) compared to Chp2 (15). However, it is unclear how these significant differences in expression levels and binding affinities between Swi6 and Chp2 extend to how both proteins interact with H3K9me in living cells.

Deletions of Swi6 and Chp2 have additive effects on epigenetic silencing. These observations suggest that Swi6 and Chp2 have distinct roles in establishing heterochromatin (13–15). The two HP1 proteins preferentially interact with different binding partners. Epe1 is a putative H3K9 demethylase that opposes H3K9 methylation (17) and interacts with Swi6 both *in vitro* and *in vivo* (18, 19). On the other hand, the SHREC complex in *S. pombe*, which consists of two major chromatin modifying enzymes—Clr3, a histone deacetylase, and Mit1, a chromatin remodeler—preferentially forms complexes with Chp2 (17, 20–22). Mit1 interacts with Chp2 both *in vitro* and *in vivo*. It is still unclear how Swi6 and Chp2 specifically and selectively recruit their respective binding partners to sites of heterochromatin formation. One possibility is that Swi6 and Chp2 first form a complex with their partner proteins (Epe1, Mit1, and Clr3) off-chromatin, then search the genome, and ultimately bind at sites that are enriched for H3K9 methylation. Cells lacking Clr4 and H3K9 methylation exhibit a significant loss in HP1-mediated protein interactions, suggesting that chromatin may play a causal role in enabling protein-protein interactions in living cells (23). Hence, an alternative model is that HP1 proteins form complexes with their binding partners at sites of heterochromatin formation rather than off-chromatin.

Immunoprecipitation followed by mass spectrometry (IP-MS) is useful to detect protein-protein interactions. Yet, the types of interactions they detect can vary depending on factors such as lysis conditions, salt concentrations, and protein abundance. As a result, these assays

may not fully represent the range of interactions that occur between proteins in living cells. Detecting protein-protein interactions after lysing cells also removes proteins from their native, complex, and crowded chromatin environment. This difference leads chromatin-associated factors to exhibit divergent properties *in vitro* versus how they behave in cells. For example, in the case of Swi6, nucleosome binding *in vivo* is inhibited, not enhanced, by interactions with nucleic acids, unlike in *in vitro* binding assays. This enhancement is because the large excess of DNA in the cell can displace Swi6 from its binding site and promote protein turnover at sites of heterochromatin formation (24). Attempts to bridge the gap between *in vitro* and *in vivo* studies such as FRET and two-color imaging measurements rely on protein-protein interactions that are infrequent and transient given the dynamic properties of chromatin-binding proteins. Additionally, FRET poses critical methodological challenges due to its limited working distance (< 10 nm) and the rare chances of spontaneous interactions between labeled molecules (25).

Single-molecule microscopy of target protein-photoactivatable fluorescent protein fusions is a powerful tool to study protein dynamics *in vivo* (26, 27). Live-cell imaging can access the interaction of histone modifiers with their chromatin substrates (24, 28, 29). When combined with critical advances in statistical inference methods for analyzing high spatiotemporal resolution imaging data (Bayesian statistics applied to single-particle tracking) (30, 31), we can map the biophysical mobility states of proteins (as measured by their diffusion coefficients) to their biochemical properties in living cells (24). Furthermore, analyzing the probabilities of transitioning between or dissociating from each detected mobility state can provide estimates of the biochemical properties for protein-protein and protein-chromatin interactions in cells (32).

Here, we use single-molecule tracking photoactivated localization microscopy to study the dynamics and interactions of the HP1 proteins—Swi6 and Chp2—and the proteins they form complexes with—Epe1, Mit1, and Clr3. Our goal here is to determine whether the mobility states of proteins can be used to infer how they form complexes within the context of native

chromatin. Based on a combination of single particle tracking measurements and mathematical modeling, we propose a mechanism for how H3K9 methylation not just encourages specific complex formation between HP1 proteins and their interactors but also suppresses the propensity of heterochromatin-associated proteins to form off-chromatin complexes. As opposed to an inert platform or scaffold to direct HP1 binding, our study rebrands chromatin as an active participant in enhancing HP1-mediated complex formation in living cells.

RESULTS

The *S. pombe* HP1 orthologs Swi6 and Chp2 exhibit distinct, non-overlapping biophysical states in living cells

We previously used single-molecule tracking to identify biophysical diffusive states that map to distinct biochemical properties of proteins in living cells (24). We measured the *in vivo* dynamics of Swi6, one of two HP1 proteins in fission yeast. We have determined that Swi6 has four distinct mobility states each of which maps to a specific biochemical property in cells (24). Here, we measured the mobility states of the second conserved HP1 protein, Chp2. We labeled the N-terminus of the endogenous copy of Chp2 with PAmCherry (PAmCherry-Chp2) but were unable to observe an appreciable number of photoactivation events for single particle tracking likely due to its low expression level. Instead, we inserted a second copy of an N-terminally labeled PAmCherry-Chp2 under the regulation of the thiamine-repressible promoters, *nmt1, nmt41*, and *nmt81* (Figure 1A, B). We first ensured that *nmt81*-dependent expression of PAmCherry-Chp2 complements *chp2*Δ cells by measuring the silencing of a *ura4+* reporter inserted at the *mat* locus (*Kint2*). If *ura4+* is silenced, cells grow on 5-fluoroorotic acid (EMMC+FOA) containing media and fail to grow on media lacking uracil (EMM-URA). We noted that *nmt81*-PAmCherry-Chp2 is functional and successfully restores *ura4+* silencing in *chp2*Δ cells (Figure 1C).

Next, we tracked individual PAmCherry-Chp2 molecules expressed from the *nmt81* promoter in *S. pombe*. PAmCherry-Chp2 was briefly photoactivated with 405-nm laser light and imaged with 561-nm laser excitation light. We repeated this measurement until all PAmCherry-Chp2 molecules that can be activated were photobleached (see Methods). The activation-excitation-imaging cycle was repeated approximately 10 – 20 times for each cell, and the single molecules were localized and tracked in the recorded fluorescence movies with the SMALL-LABS algorithm (33). We model the motion of Chp2 molecules inside the *S. pombe* nucleus as a diffusive process and thus can assign diffusion coefficients to quantify the different mobility states associated with Chp2. We define a mobility state as a subpopulation of molecules with a distinct diffusion coefficient (D). In contrast to the four mobility states that we observed in the case of PAmCherry-Swi6 (a mixture of stationary and mobile molecules), nearly all PAmCherry-Chp2 proteins in *S. pombe* are stationary (Figure S1B). Hence, our live-cell imaging data reveals a substantially different binding configuration between Swi6 and Chp2.

To investigate any potential heterogeneity in the dynamics within the observed static molecules, we applied NOBIAS, a nonparametric Bayesian framework that can objectively determine the number of mobility states giving rise to a single-molecule tracking dataset (31). We identified two mobility states associated with PAmCherry-Chp2: over 92% of the Chp2 molecules are in the low mobility state with an average diffusion coefficient, $D_{\alpha,Chp2} = 0.007$ $\mu m^2/s$ (Figure 1D) and around 7.5% of Chp2 molecules in a fast mobility state with $D_{\delta,Chp2} = 0.13$ $\mu m^2/s$. NOBIAS analysis also provides the probability of a molecule transitioning between two mobility states within its trajectory: Chp2 molecules in the fast mobility (δ) state are much more likely to transition to the slower state compared with the reverse transition (Figure 2A). These weight fractions and transition probabilities indicate that Chp2 molecules predominantly occupy the slow (α) mobility state and only a very small proportion of Chp2 molecules occupy the fast (δ) state. This slow Chp2 motion is very different from the motion of the second *S. pombe* HP1

protein, Swi6; similar Bayesian analysis using the SMAUG package found that Swi6 molecules are distributed across four distinct mobility states (24).

To determine if the dominant slow mobility state of Chp2 corresponds to H3K9me-bound Chp2, we deleted Clr4, the only H3K9 methyltransferase in *S. pombe* (34, 35). In a *clr4*Δ background, the slowest PAmCherry-Chp2 mobility state is completely absent (Figure 1E). PAmCherry-Chp2 molecules in *clr4*Δ cells switch over to the fast mobility state consistent with Chp2 proteins moving around the nucleus in an unconstrained manner (weight fraction = 56%, D_{fast} = 0.36 μm^2/s). In addition, we observed a new mobility state that we did not previously detect in *clr4*+ cells (weight fraction = 44%, D_{int} = 0.03 μm^2/s). The new mobility state most closely matches the chromatin sampling (β state) that we previously observed in the case of Swi6. Therefore, without H3K9 methylation, Chp2 exhibits a substantial degree of binding to unmethylated chromatin. In contrast, only ~10% of Swi6 molecules are in a chromatin sampling configuration with > 60% of Swi6 molecules exhibiting fast, unconstrained diffusion in *clr4*Δ cells.

The overarching goal of our studies is to measure the biochemical properties of proteins and how they form complexes in the context of living cells. The appearance of a new mobility state in *clr4*Δ cells led us to hypothesize that Chp2 protein molecules that dissociate from H3K9me engage in a substantial degree of promiscuous off-target interactions. Unlike an *in vitro* experiment, we cannot change concentrations of proteins incrementally to determine binding affinities and specificities between proteins and their cognate ligands. Instead, we used two additional *nmt* promoter variants (*nmt41* and *nmt1*) to alter the overall Chp2 levels in wild-type cells. We used western blots to quantify the differences in expression across the three promoters. The difference between Chp2 expression driven by *nmt41* and *nmt81* is approximately 50-fold (Figure S1A). In contrast, the expression level of Chp2 is over 1000-fold higher when expressed from an *nmt1* promoter compared to *nmt81*-driven expression (Figure

S1A). Hence, the promoter variants give us a substantial dynamic range in terms of Chp2 concentration to assess whether the mobility states we observed are in any way limited by substrate availability (H3K9 methylated nucleosomes in *clr4*+ cells).

The dynamics of the medium expressed (50-fold higher) PAmCherry-Chp2^{nmt41} are slightly increased compared to low expression *nmt81* driven PAmCherry-Chp2. The slow diffusive state in the low expressing PAmCherry-Chp2^{nmt81} cells splits into two states in the medium expression PAmCherry-Chp2^{nmt41} cells with D_{slow1} =0.005 μm^2/s and D_{slow2} =0.010 μm^2/s (Figure 1F). In contrast, in the highly expressed PAmCherry-Chp2^{nmt1} (over 1000-fold compared to *nmt81*), we observe that only ~15% of Chp2 is in the slow diffusive state; the remaining Chp2 molecules are in intermediate and fast states (Figure 1G). The new state we observed in the case of the high expression PAmCherry-Chp2 cells is comparable to Chp2 dynamics in a *clr4*Δ background- where Chp2 has no substrate. In this background, Chp2 molecules adopt a new mobility state that most closely resembles the chromatin sampling β state we observed previously in our Swi6 single particle measurements. Our *ura4*+ reporter-based silencing assays revealed that PAmCherry-Chp2 expressed from an *nmt41* promoter (PAmCherry-Chp2^{nmt41}) preserves *ura4*+ reporter gene silencing whereas PAmCherry-Chp2 expressed from the high expression *nmt1* promoter (PAmCherry-Chp2^{nmt1}) disrupts silencing (Figure 1C) (14). This is possibly because Chp2 outcompetes other chromodomain-containing proteins for a limiting amount of H3K9me substrate. Hence, maintaining the equilibrium of Chp2 in a low diffusion state (H3K9me dependent) preserves its heterochromatin-associated silencing functionality.

Swi6 and Chp2 both have a chromodomain that is responsible for H3K9me binding specificity (Figure 1B). We asked to what extent Swi6 competes with Chp2 to bind to H3K9 methylated nucleosomes. We imaged PAmCherry-Chp2 in cells lacking the major HP1 protein, Swi6 (*swi6*Δ*).* Like in WT cells, the majority of Chp2 molecules in *swi6*Δ cells exhibit slow mobility. However, unlike WT cells, the slow population is split into two distinct slow mobility

states with D_{slow1} = 0.005 μm^2/s and D_{slow2} = 0.010 μm^2/s, with only a very small portion in the fast state (Figure S1C). Similar to WT cells, the fast Chp2 state is very unstable: there is a high probability of transitioning out of the fast state (Figure S2B). The appearance of a split new mobility state is likely because deleting Swi6 disrupts epigenetic silencing or because Swi6 makes unknown contributions to stabilizing Chp2 binding, although our results cannot distinguish between these two possibilities. Because nonparametric Bayesian approaches are known to have the potential for over-splitting (36), we validated the existence of the two slower states of Chp2^{nmt81} in *swi6*Δ cells and in PAmCherry-Chp2^{nmt41} cells by analyzing all of our Chp2 datasets using two other different single molecule tracking methods: Dirichlet process mixture models for single-particle tracking (DPSP) (37) and Spot-On (38). Both analysis methods capture a similar increase in dynamics and significant heterogeneity in the low mobility state tracks as NOBIAS (Figure S1).

Unlike the split in the mobility state in Chp2 in *swi6*Δ cells, we observed a change in the weight fraction of molecules in the chromatin-sampling (*β*) state when imaging PAmCherry-Swi6 in *chp2*Δ cells (24). Hence, the deletions of the individual HP1 proteins have very different impacts on protein dynamics. At the extreme limit, the *nmt1* promoter-driven expression of PAmCherry-Chp2 completely displaces Swi6 from sites of heterochromatin formation. As expected, we observed labeled mNeongreen-Swi6 molecules uniformly distributed across the nucleus upon PAmCherry-Chp2^{nmt1} overexpression (Figure S1D).

Chp2 dissociates faster from the H3K9me site *in vivo* than *in vitro*

The preponderance of the stationary H3K9me-binding state for PAmCherry-Chp2^{nmt81} implies that our high-resolution single particle tracking measurements may overestimate Chp2 dissociation rates due to photobleaching. This parameter is crucial to determine Chp2 binding kinetics *in vivo* and determine the extent to which such measurements correlate with *in vitro* assays. We estimated the dissociation rate using two approaches: 1) single-molecule tracking followed by a Bayesian Synthetic Likelihood (BSL) simulation (32). This simulation-based

approach has the benefit of not being affected by experimental time-resolution limits. 2) Single-molecule time-lapse imaging at different time intervals to ensure that photobleaching did not lead to an overestimation of the dissociation rate (39).

To infer the rate constants of transitions based on the NOBIAS transition matrices, we used a Bayesian Synthetic Likelihood (BSL) algorithm, which has previously been applied to assess Swi6 dynamics (24, 32). At each step, we simulated the experimental outcome of the transitions with 0.4-ms time steps 2000 times for a set of rate constants (Figure 2B). BSL methods infer the most justifiable distribution of rate constants to estimate the value and uncertainty of the reaction rate. We applied the BSL method to analyze the output of the single-molecule tracking analysis and estimated that $k_{diss} = 0.479 \pm 0.005\ \mathrm{s}^{-1}$ (Figure 2C). We also experimentally determined Chp2 residence times and dissociation rates using single-molecule time-lapse imaging (Methods). Based on single-molecule time-lapse imaging at five different time intervals (Figure 2D), we calculated a Chp2-H3K9me disassociation rate of $k_{diss} = 0.260 \pm 0.018\ \mathrm{s}^{-1}$ and an average dwell time of 3.85 s (Figure 2E). In contrast, time-lapse imaging of Swi6 gives $k_{diss} = 0.454 \pm 0.051\ \mathrm{s}^{-1}$ and and an average dwell time of 2.20 s (Figure S2C). Both experimental approaches (single-molecule tracking and single-molecule photobleaching) measured dissociation rates more than 10-fold faster *in vivo* compared to previous *in vitro* measurements of Chp2 binding to H3K9me ($9.6 \pm 0.60 \times 10^{-3}\ \mathrm{s}^{-1}$ for me2 and $1.5 \pm 0.27\ 10^{-2}\ \mathrm{s}^{-1}$ for me3) (14). Furthermore, comparing the results for Chp2 to previously reported Swi6 dissociation results using the same BSL analysis of single-molecule tracking data (24), we find that the Chp2 dissociation rate ($0.479\ \mathrm{s}^{-1}$) is lower than that of Swi6 ($1.27\ \mathrm{s}^{-1}$). The *in vivo* time-lapse measurement of Chp2 and Swi6 disassociation rates reveal that Chp2 remains bound to H3K9me for a longer time than Swi6 *in vivo* suggesting that, in fact, Chp2 binds to H3K9me chromatin with higher affinity. Deleting Swi6 did not affect the residence time or dissociation rate of PAmCherry-Chp2^{nmt81} in *swi6*Δ cells: $k_{diss} = 0.269 \pm 0.031\ \mathrm{s}^{-1}$ and an

average dwell time of 3.72 s (Figure S2D). The similarity in disassociation rates between PAmCherry-Chp2^{nmt81} in WT cells and in *swi6*Δ cells indicates that, although deleting Swi6 perturbs Chp2 dynamics, it does not affect the intrinsic affinity between Chp2 and H3K9me chromatin.

The anti-silencing factor Epe1 co-localizes with its HP1-binding partner primarily at sites of H3K9 methylation and exhibits limited off-chromatin dynamics

Having established the baseline dynamics of two major HP1 proteins in *S. pombe*—Swi6 and Chp2—we sought to determine how HP1 proteins interact with accessory factors to facilitate heterochromatin assembly. The putative H3K9me demethylase Epe1 is a major determinant of heterochromatin stability (17, 18, 40, 41). Epe1 directly binds to Swi6 and this interaction is essential for Epe1 recruitment to sites of H3K9 methylation. Deleting Epe1 leads to both unregulated H3K9 methylation spreading and increased epigenetic inheritance (17, 19). We labeled Epe1 at the C-terminus with PAmCherry (Epe1-PAmCherry). To confirm if Epe1 molecules successfully localize at heterochromatin sites, we labeled Swi6 with mNeonGreen (mNeonGreen-Swi6) in cells and imaged the emission in the green channel (488-nm excitation) alongside Epe1-PAmCherry in the red channel (561-nm excitation). Overlaying mNeonGreen images with Epe1-PAmCherry super-resolution images indicates that Epe1 foci form at the periphery of Swi6-heterochromatin foci (Figure 3A).

To identify the mobility states associated with Epe1, we tracked single Epe1-PAmCherry molecules and inferred the number of mobility states, the diffusion coefficient, and the weight fraction for each Epe1 state. Since the interaction between Epe1 and Swi6 is direct, we expected four mobility states, similar to what we previously observed for Swi6. In contrast, we found that Epe1 has only two mobility states and that the predominant slower state (weight fraction, π_{slow} ~ 94%, $D_{slow,\ Epe1}$ = 0.008 μm^2/s) (Figure 3B). Only ~6% of Epe1 are assigned to a faster state with $D_{fast,\ Epe1}$ = 0.22 μm^2/s. The transition probabilities indicate that transitioning

from the fast state to the slow state is much more favored than the reverse transition (21% to 0.8%) (Figure 3F). These results suggest that in the presence of H3K9me, Epe1 preferentially remains in the H3K9me bound state presumably through its direct interaction with Swi6. To validate that the recruitment of Epe1 to sites of H3K9 methylation (i.e., the slow state) is dependent on Swi6, we performed single particle tracking measurements of Epe1-PAmCherry in a *swi6*Δ background. As expected, we observed a complete loss of the slow state and the appearance of a new mobility state with a higher diffusion coefficient than the slowest state that we measured in WT cells. In addition, the weight fraction for the fast state, π_{fast}, increases from 6% in the WT background to over 50% in *swi6*Δ (Figure 3D).

To determine the role of H3K9 methylation in promoting complex formation, we performed Epe1-PAmCherry single particle tracking measurements in *clr4*Δ cells. As expected, the previously observed Epe1 foci in wild-type cells disappear and Epe1-PAmCherry molecules in *clr4*Δ cells are homogeneously distributed throughout the nucleus (Figure S3C). Also, we observed a complete loss of the slowest state, consistent with the fact that neither Swi6 nor Epe1 can localize to sites of heterochromatin in the absence of their cognate H3K9 methylation ligand (Figure 3C). Remarkably, we observed that Epe1 exhibits three mobility states in *clr4*Δ cells, and the diffusion coefficients of these states perfectly align with those of Swi6 (Figure 3C). In the *clr4+* cells, where H3K9me is present, the transition out of the fast state is 26 times higher than the transition into the fast state (Figure 3F), whereas this ratio decreases to 1.9 in *clr4*Δ cells (Figure S3B). Hence, our results suggest that Epe1 and Swi6 can also directly interact with one another to form off-chromatin complexes. However, the presence of H3K9me chromatin significantly shifts the equilibrium towards a chromatin-bound state.

Finally, we performed time-lapse imaging to measure the Epe1 dissociation rate. We estimated that Epe1 dissociates from sites of heterochromatin formation at a rate that is $k_{diss} = 0.288 \pm 0.044\ s^{-1}$ according to single-molecule time-lapse imaging with four time intervals

(Figure 3E). Consistently, BSL analysis of the single-molecule tracking transition matrix gave $k_{diss} = 0.236 \pm 0.003\ s^{-1}$(Figure 3F) or a dwell time of 4.24s. These data suggest that Epe1 remains bound to heterochromatin for dwell times that are much longer than that of Swi6 despite Swi6 and Epe1 directly interacting with each other to form a complex. These long dwell times suggest that H3K9me or multivalency arising from Swi6 oligomerization might promote the stable association of Epe1 at sites of heterochromatin formation.

The histone remodeler Mit1 and the histone deacetylase Clr3 assemble into the SHREC complex only at heterochromatin

Given our observation that Epe1 and Swi6 preferentially form complexes at sites of H3K9 methylation and not off-chromatin, we wanted to determine the extent to which the principle of H3K9me-directed complex assembly might be generalizable to other HP1 protein complexes. The SHREC complex consists of a histone remodeler Mit1 and histone deacetylase (HDAC) Clr3 (Figure 4A) (20, 21). Unlike Epe1, which depends on Swi6 for its recruitment to heterochromatin, proteins that are part of the SHREC complex preferentially form complexes with Chp2 (13, 21). The C-terminus of Chp2 forms a complex with the N-terminus of Mit1, and their interactions have been characterized using X-ray crystallography (21). These interactions are further supported by studies of Swi6 purification in *chp2*Δ cells: mass spectrometry reveals a precipitous loss of Mit1 from heterochromatin (23). The recruitment of Clr3 is more complex and relies both on HP1-dependent and HP1-independent interactions (13, 21, 42).

We previously determined that Chp2 exhibits two distinct mobility states and hence we extended our studies to identify the mobility states associated with its primary interacting partners: Mit1 and Clr3. We fused PAmCherry to the N-terminus of Mit1 and Clr3 and expressed the two fusion proteins using a thiamine-repressible *nmt81* promoter. We determined that PAmCherry-Mit1^{nmt81} preserved epigenetic silencing at the *mat* locus by using a *ura4*+-based silencing assay (Figure S4A). As previously described, the establishment of *ura4*+ silencing

leads to growth in FOA -containing media (EMMC+FOA) and no growth in media without uracil (EMM-URA). Our single-molecule tracking data for PAmCherry-Mit1^{nmt81} and PAmCherry-Clr3^{nmt81} reveals that both proteins exhibit three mobility states (Figure 4B). The diffusion coefficients for Mit1 and Clr3 only match each other for the slowest states (D_{slow} = 0.005 μm^2/s) with comparable weight fractions. 28% of the single-molecule steps are slow for Mit1 and 25% for Clr3. Notably, the D_{slow} values for these two proteins are again at levels similar to what we have observed in the case of other heterochromatin-associated factors (D_{slow} of Swi6, Chp2, and Epe1). The density heatmap of reconstructed single-molecule fits for Mit1 shows that the Mit1 high-density hotspots also exhibit spatial patterns that are similar to Chp2, Swi6, and Epe1, while Clr3 has a more dispersed pattern (Figure S4C).

We analyzed transition probabilities and calculated spatial autocorrelations for Mit1 and Clr3 based on our single-molecule tracking data. We noticed that Clr3 has a higher transition probability from the fast state to the intermediate state compared with Mit1 (Figure 4D, E). Spatial autocorrelation analysis is useful, especially when combined with the state label NOBIAS provides for each step. We used a Ripley's H function to determine the spatial overlap between Mit1 and Clr3 for different mobility states (43). A higher H(*r*) value indicates a higher clustering level at searching radius *r*, and Mit1 has a higher H function value than Clr3 in the intermediate state at all searching radii (Figure 4C). In contrast, there is little difference between the H functions for the slowest states of Mit1 and Clr3, indicating that the clustering level of the Mit1 and Clr3 slow states is similar (Figure S4B). In summary, the spatial auto-correlation analysis and single-molecule dynamic measurements for Mit1 and Clr3 suggest that the SHREC complex components preferentially co-localize on chromatin and is unlikely to form off-chromatin complexes in live *S. pombe* cells.

Whether Chp2 and Mit1 recruit the HDAC module Clr3 to sites of H3K9me or the two SHREC complex components are recruited to the H3K9me site independently remains an open question (13, 21). To test between these possibilities, we deleted Clr1, a protein in the SHREC

complex that is thought to link the remodeling and HDAC modules. We observed an increase in the fast state weight fraction and a decrease in the bound state weight fraction for Mit1 (Figure S4D), which further confirmed that Mit1's bound state depends on heterochromatin as Clr1 also interacts with Chp2 (13). We also acquired and analyzed single-molecule tracking data for PAmCherry-Mit1 in *clr3*Δ cells, in which the number of diffusive states remains 3, and there is little change in the corresponding *D* value or weight fraction for each state (Figure S4E), which means the binding of the remodeler module (Mit1) does not depend on the HDAC module (Clr3). In contrast, we found that the slow state of PAmCherry-Clr3 in *mit1*Δ cells has a decreased weight fraction and an increase in the diffusion coefficient associated with the slow state (D_{slow} changes from 0.005 μm^2/s to 0.010 μm^2/s) (Figure S4F). These results suggest that Clr3 binding might depend on the successful binding and recruitment of Mit1. Alternatively, the deletion of Mit1 could have a larger effect on heterochromatin stability but our imaging experiments cannot distinguish between these two possibilities.

SHREC complex dynamics are affected by H3K9 methylation

To test whether the slowest mobility state corresponding to Mit1 and Clr3 depends on H3K9 methylation, we performed single-molecule tracking measurements in *clr4*Δ cells. In *clr4*Δ cells, Mit1 and Clr3 exhibit a substantial increase in the fastest mobility state (17.7% to 37.8% for Mit1 and 20.0% to 46.0% for Clr3) with a concomitant decrease in the slowest mobility state (28.4% to 10.7% for Mit1 25.5% to 13.0% for Clr3) (Figure 5A-B). However, unlike what we observed in the case of the two HP1 proteins—Swi6 and Chp2—or Epe1, the slowest mobility state is not fully eliminated for either PAmCherry-Mit1 or PAmCherry-Clr3 in *clr4*Δ cells. These results suggest that other mechanisms in addition to H3K9 methylation are responsible for the slow mobility state of Mit1 and Clr3 (although more than half of its bound state is determined by H3K9 methylation). In the Ripley's H cluster analysis, for all steps of Mit1 and Clr3 in WT cells and *clr4*Δ cells, we notice a substantial decrease in H(*r*) value for both proteins in the absence

of Clr4, consistent with reduced clustering (Figure 5C). Reconstructed localization maps of PAmCherry-Mit1 and PAmCherry-Clr3 in *clr4*Δ cells also show overall unclustered spatial patterns for both proteins (Figure 5D).

Next, we tested the extent to which the slow mobility state of Mit1 and Clr3 depends on the two HP1 proteins- Swi6 and Chp2. We tracked single molecules of PAmCherry-Mit1 in *chp2*Δ, *swi6*Δ, and *swi6*Δ*chp2*Δ cells. We analyzed the Mit1 single particle trajectories associated with each dataset and inferred the number of diffusive states and associated D and π values (Figures 5E-F, S5A). We notice that Mit1 in *chp2*Δ cells exhibits a substantial decrease in the bound state weight fraction compared to WT cells, but this decrease is less than what we observed in the case of *clr4*Δ cells (Figure 5E). In contrast, we observed a similar weight fraction for all three diffusive states of Mit1 in *swi6*Δ cells compared to Mit1 in WT cells (Figure S5A). These results suggest and confirm that Chp2 is the primary HP1 protein interacting with Mit1. In the absence of Chp2, Swi6 can play a compensatory role highlighting the potential for cross-talk and shared binding sites between the two proteins. Indeed, we observed that Mit1 dynamics in *swi6*Δ*chp2*Δ produced an additive effect, resulting in a further decreased bound state weight fraction compared with only *chp2*Δ cells (Figure 5F).

For the HDAC Clr3, we acquired single-molecule tracking data for PAmCherry-Clr3 in *chp2*Δ and *swi6*Δ cells. In the analysis of Clr3 in *chp2*Δ cells (Figure S5B), we noticed the same decrease in the bound state as for Mit1 in *chp2*Δ cells, which supports the hypothesis of Chp2-mediated HDAC recruitment. Interestingly, in *swi6*Δ cells (Figure S5C), we observe not only a decreased weight fraction for the Clr3 bound state, but also an increased D_{slow} from 0.005 μm^2/s to 0.010 μm^2/s. Our data shows that the stable nucleosome-bound state of the HDAC component Clr3, requires H3K9me, Chp2, and Mit1. We thus infer that the two modules of the SHREC complex only co-localize in presence of H3K9me and HP1 proteins at heterochromatin

sites, given the substantial differences in recruitment behavior between the remodeler component and the HDAC component of the SHREC complex.

DISCUSSION

We used single-particle tracking approaches to investigate how heterochromatin-associated factors form complexes in living fission yeast cells. Our observations of the properties of heterochromatin-associated proteins in cells deviate in important and substantive ways from *in vitro* studies. Previous studies have shown that Swi6 binds to nucleosomes with a 3-fold higher affinity than Chp2 (15). In contrast, our data based on 1) the weight fractions of molecules in the H3K9 methylation-dependent slow mobility state, 2) the transition rates of molecules between the free and bound states, and 3) time-lapse imaging to measure k_{off} demonstrates that the majority of Chp2 molecules are in the H3K9 methylation-bound state and Chp2 binds with higher affinity to H3K9me chromatin. By varying Chp2 protein expression levels, we also revealed how Chp2 binds with exquisite specificity to H3K9me chromatin when expressed in limiting (and physiologically relevant) amounts. Hence, despite the two HP1 proteins having very similar domains, their different amino acid compositions, especially within the nucleic acid binding hinge domain, likely leads to different biochemical interactions in cells. These results might explain why Chp2 is not easily displaced by Swi6 despite the levels of Chp2 protein being 100-fold lower than that of Swi6 in cells.

In our earlier work, we noted that deleting Chp2 had little effect on the overall dynamics of Swi6 with a slight increase in the chromatin binding (β state) (24). We concluded that this limited dependence was likely because H3K9me is not substrate-limiting in cells. Yet, deleting Swi6 leads to increased dynamics and the emergence of a new diffusive state for Chp2. The increased dynamics and the new Chp2-associated mobility state might appear either because 1) Swi6 oligomerization may stabilize Chp2 binding at sites of heterochromatin formation. This possibility would also explain the differences between H3K9me binding we observed in the *in vitro* and *in vivo* data for Swi6 relative to Chp2; or because 2) Swi6 is not directly involved in

Chp2-H3K9me binding, but the loss of Swi6 results in an overall reduction in heterochromatin stability, making Chp2 less bound.

The binding properties of the two HP1 proteins- Swi6 and Chp2, serve as an important point of departure for our measurements on heterochromatin complex assembly in living cells. Epe1, a major anti-silencing factor that interacts with Swi6, exhibits only two mobility states suggesting that Epe1 interacts with Swi6 exclusively at sites of H3K9 methylation. These studies are consistent with our earlier observations showing that the addition of an H3K9 methylated peptide to *in vitro* binding assays dramatically increased the extent of binding between Epe1 and Swi6 (41). Swi6 IP-MS studies also show that Epe1 interacts with Swi6 in *clr4+* but not *clr4*Δ or H3K9R mutants (41). Indeed, our studies precisely define that it is in fact the presence of H3K9 methylation itself that attenuates other non-productive Epe1-Swi6 interaction states. Deleting Clr4 leads to Epe1 exhibiting three mobility states, the diffusion coefficients of which perfectly align with that of Swi6 in *clr4*Δ cells. Hence, Swi6 and Epe1 likely form off-chromatin complexes and bind directly to each other. However, the presence of H3K9 methylation dramatically shifts the equilibrium populations toward a chromatin-bound state.

We tested whether the principle of H3K9 methylation enhancing complex formation could be extended to other proteins such as the chromatin remodeler, Mit1, and the histone deacetylase, Clr3, both of which form complexes with the second HP1 protein, Chp2. Unlike Chp2, which has only two mobility states, Mit1 and Clr3 exhibit three mobility states. Both Mit1 and Clr3 exhibit mobility states with different diffusion coefficients and spatial autocorrelation functions except for the slow state which we attribute to an H3K9 methylation bound fraction. These results suggest that Mit1 and Clr3, which are components of the SHREC complex, co-localize only at sites of H3K9 methylation. Our results are consistent with recent structural work on SHREC complex proteins highlighting the special role that Chp2 has in recruiting Mit1 to heterochromatin (21, 22). These results suggest alternative modes of SHREC complex

component recruitment which eventually lead to the co-localization of the remodeler and deacetylase modules, binding as independent components. For example, Mit1 can be recruited via HP1-dependent interactions, CD domain-dependent nucleic acid interactions like DNA binding proteins at the telomeres (20, 44). Clr3, the HDAC module, interacts with Clr2 which has an MBD domain that binds to nucleic acids and also directly interacts with DNA-binding proteins such as Atf1 and Pcr1 (21). Hence, the availability of different binding partners that associate with the SHREC complex could lead to a low mobility state of Mit1 and Clr3, even in the absence of H3K9 methylation.

Chromatin is largely thought to be merely a scaffold that recruits histone-binding proteins to particular locations in the genome (45). Our single-molecule imaging measurements of heterochromatin proteins and their binding partners reveal a vital role for H3K9 methylation as an enhancer of complex formation in living cells. Although the proteins whose properties we measured directly bind to each other and form pairwise interactions *in vitro,* we observed little off-heterochromatin co-localization when H3K9 methylation is present. Our results reveal the dramatic shift in the equilibrium binding states induced by the presence of H3K9 methylation. Our results have important implications for the reconstitution and structural biology of heterochromatin-associated factors. Specifically, our results emphasize the need to explicitly include H3K9 methylated chromatin substrates when describing models of how heterochromatin-associated factors form complexes both *in vitro* and in cells given its role in enhancing complex formation. Although the mechanisms of such enhancement are not well understood, it is likely due to protein conformational changes that are triggered by nucleosome binding and H3K9 methylation that switches heterochromatin associated proteins from a low-affinity to a high affinity interaction state (41).

MATERIALS AND METHODS

Plasmids

All fluorescently tagged proteins were made with Gibson cloning. Strains with *nmt* promoters were constructed by modifying existing pDual plasmids (46).

Strains

Most strains were constructed using PCR-based gene-targeting approach (47). All strains with a PAmCherry fluorescent tag were made by constructing pDual vectors, containing the specified *nmt* promoter and the indicated protein (46). The plasmid was digested with the restriction enzyme NotI, and the cut plasmid was transformed into *leu1-32* strains to select for growth on EMM-leu media (minimal media lacking leucine) as the pDual vector restores a functional *leu1+* gene. Epe1-PAmCherry was made by using long oligos to tag Epe1. Deletions were made by PCR-based gene targeting approach or a cross followed by random spore analysis (48). All strains in this study are listed in Table S1.

S. pombe live-cell imaging

Yeast strains were grown in standard complete YES media (US Biological, cat. Y2060) containing the full complement of yeast amino acids and incubated overnight at 32°C. For PAmCherry-Epe1 strains and Epe1 mutants under the control of the native Epe1 promoter, the seed culture was diluted into the same YES media and incubated at 25 °C with shaking to reach OD_{600} ~ 0.5. For strains with the *nmt1*, *nmt41*, or *nmt81* promoter, the seed culture was diluted into EMMC media (FORMEDIUM, cat. PMD0402) containing the full complement of yeast amino acids and incubated at 30 °C with shaking to reach OD_{600} ~ 0.5. To maintain cells in the exponential phase and eliminate extranuclear vacuole formation, the culture was maintained at OD_{600} ~ 0.5 for two days with dilutions performed at ~12-hour time intervals (~24-hour time intervals for EMM media culture). Cells were pipetted onto a pad of 2% agarose prepared in EMM media and each agarose pad sample was imaged for less than 1 hour. *S. pombe* cells were imaged at room temperature with a 100× 1.40 NA oil immersion objective. The fluorescent

background was decreased by exposure to 488-nm light (Coherent Sapphire, 377 W/cm^2 for 20 – 40 s). A 406-nm laser (Coherent Cube 405-100; 1-5 W/cm^2) was used for photoactivation (200 ms activation time) and a 561-nm laser (Coherent-Sapphire 561-50; 70.7 W/cm^2) was used for excitation. Images were acquired at 40-ms exposure time per frame. The fluorescence emission was filtered to eliminate the 561-nm excitation source and imaged using a 512 × 512-pixel Photometrics Evolve EMCCD camera.

Silencing assays

Strains containing the *ura4+* reporter were grown overnight. Cells were equalized to 1OD/ml then four tenfold dilutions were spotted on minimal nonselective media (EMMC), minimal media lacking uracil (EMM-URA), or minimal media containing 5FOA (EMMC+FOA). 5-flouro-oratic acid (5-FOA) was added at a concentration of 1g/L in EMMC+FOA plates. The plates were incubated at 32 °C for 3-4 days before imaging.

Single-molecule trajectory analysis

Recorded PAmCherry single-molecule positions were localized and tracked with SMALL-LABS software (33). A mask of the nucleus of each cell was determined based on auto-florescence outside the nucleus in the 488nm bleaching step. Only the signal within the nucleus mask was analyzed. Single-molecule trajectory datasets were analyzed by a nonparametric Bayesian framework NOBIAS to infer the number of mobility states, the parameter for each state, and the transition between states (31). More than 1000 trajectories for each SPT dataset are put in the framework for robust analysis and to eliminate rare events. Reported parameters for each state are the posterior mean after the number of mobility states stabilizes, and reported uncertainty is the standard deviation from the posterior distribution. Some datasets were also analyzed with two publicly available SPT analysis software DPSP (37) and Spot-On (38). In DPSP analysis, the chosen range of diffusion coefficients was 10^{-3} – 10 μm^2/s. In Spot-On analysis, the number of components was set to 2 and 3 separately.

Clustering Analysis for the Swi6 Distributions

The spatial pattern of each mobility state was investigated using the Ripley's *K* function (43):

$$K(r) = \lambda^{-1} \sum_{i=1}^{n} \sum_{i \neq j} \frac{I(r_{ij} < r)}{n}$$

Where *r* is the search radius, *n* is the number of points in the set, λ is the point density and, r_{ij} is the distance between the *i*th and *j*th point. $I(x)$ is an indicator function. K(*r*) is further normalized to obtain the Ripley's H function:

$$H(r) = \left(\frac{K(r)}{\pi}\right)^{\frac{1}{2}} - r$$

In this function, $H(r) = 0$ stands for a random distribution, $H(r) > 0$ means a clustered spatial pattern, and $H(r) < 0$ means a dispersed pattern. In the analysis, the nucleus was approximated as a circle to determine the area and perform edge correction (49). We calculated H(*r*) for each cell, then we calculated an overall H(*r*) from the average of all cells weighted by the fit densities.

To eliminate effects from the spatial correlation between single-molecule steps within the same trajectories, we simulated diffusion trajectories with similar confined area size, average track length, and overall density as experimental trajectories by drawing step lengths from the step size distribution of the corresponding experiment steps. This normalization is reported in previous work (24).

Reconstructed single-molecule heatmap

For each cell, the nucleus and cell outlines were obtained from the fluorescence image of the nucleus and the phase-contrast image of the cell, respectively; these outlines were then approximated by a circle and a rectangle with circular caps, respectively. Every frame was analyzed by SMALL-LABS to identify single molecules, and the position and frame number of every single molecule were saved. To generate the reconstructed single-molecule heatmap for the cell, the pixel intensities after subtraction of the fitted offset in the appropriate diffraction-

limited region about each single molecule were summed and the sum of all well-fit molecules was globally normalized.

Fine-grained chemical rate constant inference

To infer the rate constants of transition for each of these proteins, we used a Bayesian Synthetic Likelihood algorithm similar to the one previously reported for the Swi6 rate constants (24). At each step, we began with a set of rate constants and their posterior density. We then proposed a potential new set in one of three ways based on a t-distributed random variable, *T*, with 10 degrees of freedom and the number of protein states *N*: we multiplied a random rate by $\exp(0.02T)$, we multiplied every rate by $\exp(0.02T/N^2)$, or we multiplied a random pair of opposing rates by $\exp(0.01T)$. We simulated the experimental outcome of the transitions 2000 times for a set of rate constants. We used these simulations to calculate a likelihood distribution for the rate constants, multiplied the result by an improper Jeffries prior ($P(rate) \propto 1/rate$), and compared the posterior density to that of the older set of rate constants using the standard Metropolis Hastings algorithm to decide whether to keep the old set of rates or accept the new one. We first simulated our system by dividing the experimental time (0.04 sec) into 100-time steps $\delta t = 4\times10^{-4}$ sec. We assumed that the sampled proteins were partitioned across states according to their equilibrium proportions based on their reported transition matrices from the NOBIAS single-molecule tracking analysis. We sampled from a binomial distribution with transition probability as given above and the number of molecules in a state to determine the number of molecules that transitioned. The posterior mean reaction rates were considered the final posterior rates. We report them with a 95% highest density credible interval.

Single-molecule time-lapse imaging

We model the binding of Chp2 and H3K9me or Swi6 to Epe1 as a direct two-component association/disassociation reaction:

$$AB \leftrightharpoons A + B$$

The measured residence time of each PAmCherry-Chp2 or PAmCherry-Epe1 molecule was estimated from the lifetime of the stationary fluorescence signal. k_{app_diss} was acquired by fitting the probability distribution function, P, of the measured residence times, $\tau_{measured}$, to a single exponential decay function:

$$P = \exp\left(-k_{app\_diss} \cdot \tau_{measured}\right)$$

The measured apparent disassociation rate, k_{app_diss}, consists of the true disassociation rate, k_{diss}, and the photobleaching rate of the PAmCherry label, $k_{bleaching}$; we separated these contributions by collecting data at multiple delay times to measure the photobleaching rate. For static molecules, we introduced a dark period with each time interval to keep the integration time, τ_{int}, the same and introduced different lengths of dark delay times, τ_{delay}. In this way, the contribution of photobleaching was kept the same for different total time intervals, $\tau_{TL} = \tau_{int} + \tau_{delay}$. We measured the residence time $\tau_{measured} = (n-1)\tau_{TL}$ by counting the total number of sequential frames, n, in which the molecule was detected. Finally, the true disassociation rate, k_{diss}, was estimated from a linear regression of the two-term relationship (39):

$$k_{app\_diss}\tau_{TL} = \tau_{TL}k_{diss} + \tau_{int}k_{bleaching}$$

This linear regression also took the uncertainty of each data point from the exponential fitting into consideration and gives the final fitted slope k_{diss} and its uncertainty.

Acknowledgments: We thank Danesh Moazed for sharing fission yeast strains used in this study. This work was funded by a National Science Foundation Understanding Rules of Life Award (1921677) to JSB, PF, and KR, and NIH award R35GM137832 to KR. This work used the Extreme Science and Engineering Discovery Environment (XSEDE) comet resource at the San Diego Supercomputing Center through allocation TG-MCB140220 to PF (Towns et al., 2014).

References

1. C. D. Allis, T. Jenuwein, The molecular hallmarks of epigenetic control. *Nat Rev Genet* **17**, 487–500 (2016).

2. S. I. S. Grewal, S. Jia, Heterochromatin revisited. *Nat Rev Genet* **8**, 35–46 (2007).
3. S. I. S. Grewal, D. Moazed, Heterochromatin and Epigenetic Control of Gene Expression. *Science* **301**, 798–802 (2003).
4. A. Verdel, *et al.*, RNAi-Mediated Targeting of Heterochromatin by the RITS Complex. *Science* **303**, 672–676 (2004).
5. S. A. Jacobs, S. Khorasanizadeh, Structure of HP1 Chromodomain Bound to a Lysine 9-Methylated Histone H3 Tail. *Science* **295**, 2080–2083 (2002).
6. S. A. Jacobs, *et al.*, Specificity of the HP1 chromo domain for the methylated N-terminus of histone H3. *EMBO J* **20**, 5232–5241 (2001).
7. D. Canzio, A. Larson, G. J. Narlikar, Mechanisms of functional promiscuity by HP1 proteins. *Trends in Cell Biology* **24**, 377–386 (2014).
8. S. Sanulli, J. D. Gross, G. J. Narlikar, Biophysical Properties of HP1-Mediated Heterochromatin. *Cold Spring Harb Symp Quant Biol* **84**, 217–225 (2019).
9. S. Rea, *et al.*, Regulation of chromatin structure by site-specific histone H3 methyltransferases. *Nature* **406**, 593–599 (2000).
10. G. Thon, J. Verhein-Hansen, Four Chromo-domain Proteins of *Schizosaccharomyces pombe* Differentially Repress Transcription at Various Chromosomal Locations. *Genetics* **155**, 551–568 (2000).
11. D. Halverson, G. Gutkin, L. Clarke, A novel member of the Swi6p family of fission yeast chromo domain-containing proteins associates with the centromere in vivo and affects chromosome segregation. *Mol Gen Genet* **264**, 492–505 (2000).
12. A. J. Bannister, *et al.*, Selective recognition of methylated lysine 9 on histone H3 by the HP1 chromo domain. *Nature* **410**, 120–124 (2001).
13. M. R. Motamedi, *et al.*, HP1 Proteins Form Distinct Complexes and Mediate Heterochromatic Gene Silencing by Nonoverlapping Mechanisms. *Molecular Cell* **32**, 778–790 (2008).
14. M. Sadaie, *et al.*, Balance between Distinct HP1 Family Proteins Controls Heterochromatin Assembly in Fission Yeast. *MCB* **28**, 6973–6988 (2008).
15. R. S. Isaac, *et al.*, Biochemical Basis for Distinct Roles of the Heterochromatin Proteins Swi6 and Chp2. *Journal of Molecular Biology* **429**, 3666–3677 (2017).
16. N. P. Cowieson, J. F. Partridge, R. C. Allshire, P. J. McLaughlin, Dimerisation of a chromo shadow domain and distinctions from the chromodomain as revealed by structural analysis. *Current Biology* **10**, 517–525 (2000).
17. N. Ayoub, *et al.*, A Novel jmjC Domain Protein Modulates Heterochromatization in Fission Yeast. *MCB* **23**, 4356–4370 (2003).
18. M. Zofall, S. I. S. Grewal, Swi6/HP1 Recruits a JmjC Domain Protein to Facilitate Transcription of Heterochromatic Repeats. *Molecular Cell* **22**, 681–692 (2006).
19. K. Ragunathan, G. Jih, D. Moazed, Epigenetic inheritance uncoupled from sequence-specific recruitment. *Science* **348**, 1258699 (2015).
20. T. Sugiyama, *et al.*, SHREC, an Effector Complex for Heterochromatic Transcriptional Silencing. *Cell* **128**, 491–504 (2007).
21. G. Job, *et al.*, SHREC Silences Heterochromatin via Distinct Remodeling and Deacetylation Modules. *Molecular Cell* **62**, 207–221 (2016).
22. K. Leopold, A. Stirpe, T. Schalch, Transcriptional gene silencing requires dedicated interaction between HP1 protein Chp2 and chromatin remodeler Mit1. *Genes Dev.* **33**, 565–577 (2019).
23. N. Iglesias, *et al.*, Native Chromatin Proteomics Reveals a Role for Specific Nucleoporins in Heterochromatin Organization and Maintenance. *Molecular Cell* **77**, 51-66.e8 (2020).

24. S. Biswas, *et al.*, HP1 oligomerization compensates for low-affinity H3K9me recognition and provides a tunable mechanism for heterochromatin-specific localization. *Sci. Adv.* **8**, eabk0793 (2022).
25. D. W. Piston, G.-J. Kremers, Fluorescent protein FRET: the good, the bad and the ugly. *Trends in Biochemical Sciences* **32**, 407–414 (2007).
26. A. Gahlmann, W. E. Moerner, Exploring bacterial cell biology with single-molecule tracking and super-resolution imaging. *Nat Rev Microbiol* **12**, 9–22 (2014).
27. A. Kusumi, T. A. Tsunoyama, K. M. Hirosawa, R. S. Kasai, T. K. Fujiwara, Tracking single molecules at work in living cells. *Nat Chem Biol* **10**, 524–532 (2014).
28. A. Ranjan, *et al.*, Live-cell single particle imaging reveals the role of RNA polymerase II in histone H2A.Z eviction. *eLife* **9**, e55667 (2020).
29. S. Basu, *et al.*, Live-cell 3D single-molecule tracking reveals how NuRD modulates enhancer dynamics. *bioRxiv*, 2020.04.03.003178 (2021).
30. J. D. Karslake, *et al.*, SMAUG: Analyzing single-molecule tracks with nonparametric Bayesian statistics. *Methods*, S1046202320300293 (2020).
31. Z. Chen, L. Geffroy, J. S. Biteen, NOBIAS: Analyzing Anomalous Diffusion in Single-Molecule Tracks With Nonparametric Bayesian Inference. *Front. Bioinform.* **1**, 742073 (2021).
32. S. N. Wood, Statistical inference for noisy nonlinear ecological dynamic systems. *Nature* **466**, 1102–1104 (2010).
33. B. P. Isaacoff, Y. Li, S. A. Lee, J. S. Biteen, SMALL-LABS: Measuring Single-Molecule Intensity and Position in Obscuring Backgrounds. *Biophysical Journal* **116**, 975–982 (2019).
34. K. Ekwall, *et al.*, Mutations in the fission yeast silencing factors clr4+ and rik1+ disrupt the localisation of the chromo domain protein Swi6p and impair centromere function. *Journal of Cell Science* **109**, 2637–2648 (1996).
35. A. V. Ivanova, M. J. Bonaduce, S. V. Ivanov, A. J. S. Klar, The chromo and SET domains of the Clr4 protein are essential for silencing in fission yeast. *Nat Genet* **19**, 192–195 (1998).
36. E. B. Fox, E. B. Sudderth, M. I. Jordan, A. S. Willsky, An HDP-HMM for systems with state persistence in *Proceedings of the 25th International Conference on Machine Learning - ICML '08*, (ACM Press, 2008), pp. 312–319.
37. A. Heckert, L. Dahal, R. Tijan, X. Darzacq, Recovering mixtures of fast-diffusing states from short single-particle trajectories. *eLife* **11**, e70169 (2022).
38. A. S. Hansen, *et al.*, Robust model-based analysis of single-particle tracking experiments with Spot-On. *eLife* **7**, e33125 (2018).
39. J. C. M. Gebhardt, *et al.*, Single-molecule imaging of transcription factor binding to DNA in live mammalian cells. *Nat Methods* **10**, 421–426 (2013).
40. K. Bao, C.-M. Shan, J. Moresco, J. Yates, S. Jia, Anti-silencing factor Epe1 associates with SAGA to regulate transcription within heterochromatin. *Genes Dev.* **33**, 116–126 (2019).
41. G. Raiymbek, *et al.*, An H3K9 methylation-dependent protein interaction regulates the non-enzymatic functions of a putative histone demethylase. *eLife* **9**, e53155 (2020).
42. M. Zofall, R. Sandhu, S. Holla, D. Wheeler, S. I. S. Grewal, Histone deacetylation primes self-propagation of heterochromatin domains to promote epigenetic inheritance. *Nat Struct Mol Biol* **29**, 898–909 (2022).
43. B. D. Ripley, The second-order analysis of stationary point processes. *Journal of Applied Probability* **13**, 255–266 (1976).
44. K. M. Creamer, *et al.*, The Mi-2 Homolog Mit1 Actively Positions Nucleosomes within Heterochromatin To Suppress Transcription. *Mol Cell Biol* **34**, 2046–2061 (2014).

45. S. D. Taverna, H. Li, A. J. Ruthenburg, C. D. Allis, D. J. Patel, How chromatin-binding modules interpret histone modifications: lessons from professional pocket pickers. *Nat Struct Mol Biol* **14**, 1025–1040 (2007).
46. A. Matsuyama, *et al.*, pDUAL, a multipurpose, multicopy vector capable of chromosomal integration in fission yeast. *Yeast* **21**, 1289–1305 (2004).
47. J. Bähler, *et al.*, Heterologous modules for efficient and versatile PCR-based gene targeting inSchizosaccharomyces pombe. *Yeast* **14**, 943–951 (1998).
48. S. Torres-Garcia, *et al.*, SpEDIT: A fast and efficient CRISPR/Cas9 method for fission yeast. *Wellcome Open Res* **5**, 274 (2020).
49. F. Goreaud, R. Pélissier, On explicit formulas of edge effect correction for Ripley's *K* -function. *Journal of Vegetation Science* **10**, 433–438 (1999).

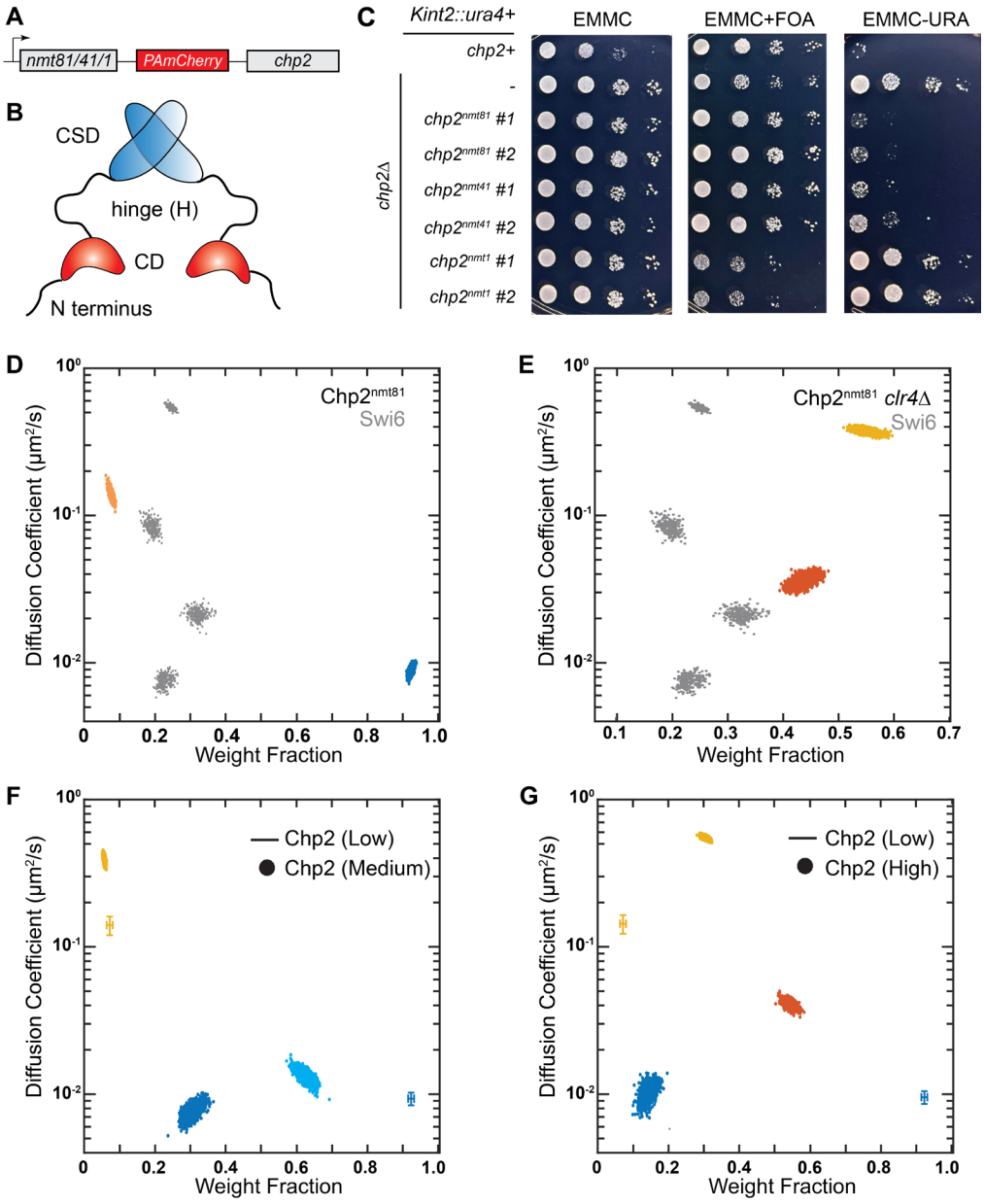

Figure 1. Single-molecule dynamics of PAmCherry-Chp2 at different concentrations. A: PAmCherry is fused to the N-terminus of Chp2 and expressed ectopically using a series of inducible promoters: *nmt1*, *nmt41*, and *nmt81*. **B**: Schematic of the Chp2 domains. CD: chromodomain (H3K9me recognition); H: hinge (nucleic acid binding); CSD: chromoshadow domain (dimerization interface). **C**: Silencing assay using an *ura4+* reporter inserted at the mat locus (*Kint2::ura4).* 10-fold serial dilutions of cells expressing Chp2 from different *nmt* promoters were plated on EMMC, EMMC +FOA, and EMM-URA plates. **D-E**: NOBIAS identifies two distinct mobility states for PAmCherry-Chp2^{nmt81}. Each colored point is the average single-molecule diffusion coefficient of PAmCherry-Chp2 molecules in that state sampled from the posterior distribution of NOBIAS inference at a saved iteration after convergence in WT cells (**D**) and *clr4Δ* cells (**E**). Grey points are the previously reported PAmCherry-Swi6 single-molecule dynamics (24). **F-G**: NOBIAS identifies multiple mobility states for PAmCherry-Chp2^{nmt41} (medium expression, **F**) and PAmCherry-Chp2^{nmt1} (high expression, **G**). Each colored point is the average single-molecule diffusion coefficient sampled from the posterior distribution for PAmCherry-Chp2 at the indicated expression level. Colored crosses represent the data from PAmCherry-Chp2^{nmt81} (low expression; data in **D**).

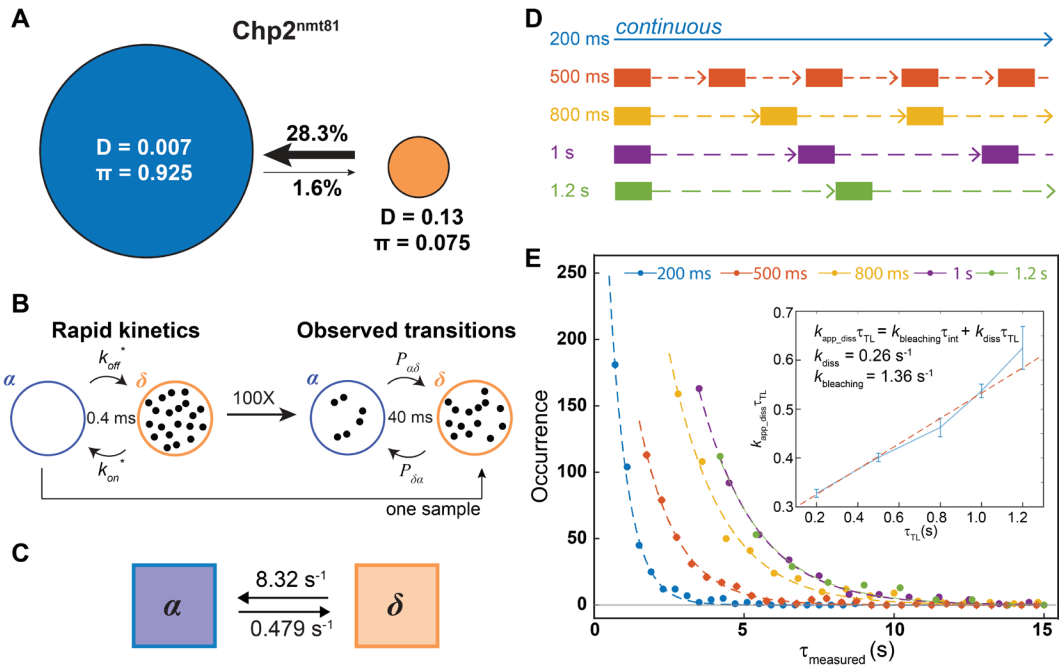

Figure 2. PAmCherry-Chp2 rate constants inferred from fine-grained chemical kinetic simulations and single-molecule time-lapse imaging. A: Inferred transition probabilities between the two mobility states of PAmCherry-Chp2^{nmt81} from single-molecule tracking (Figure **1D**). Diffusion coefficients, *D*, in units of μm^2/s and weight fractions, π, are indicated. Arrow widths are proportional to the transition probabilities. **B**: Fine-grained chemical kinetic simulations with Bayesian Synthetic Likelihood algorithm. The reaction on/off rate is proposed and simulated at a 0.4-ms time interval to calculate the likelihood based on transition probabilities from **A** at the 40-ms experimental imaging time interval. **C:** Inferred rate constants for PAmCherry-Chp2^{nmt81}. **D:** Schematic of single-molecule time-lapse imaging. The time-lapse period, τ_{TL}, is the sum of the 200-ms integration time and the time delay. Five different time delays were introduced to access τ_{TL} = 200, 500, 800, 1000, and 1200 ms. **E**: Dwell time distributions for PAmCherry-Chp2^{nmt81}. The distributions are shown with fits to an exponential decay. Insert: linear fit (red dashed line) of $k_{app\_diss}\tau_{TL}$ vs. τ_{TL}, from which the dissociation rate constant, k_{diss}, and the photobleaching rate constant, $k_{bleaching}$, are obtained. Errors bars are the standard deviation of the exponential decay fitting.

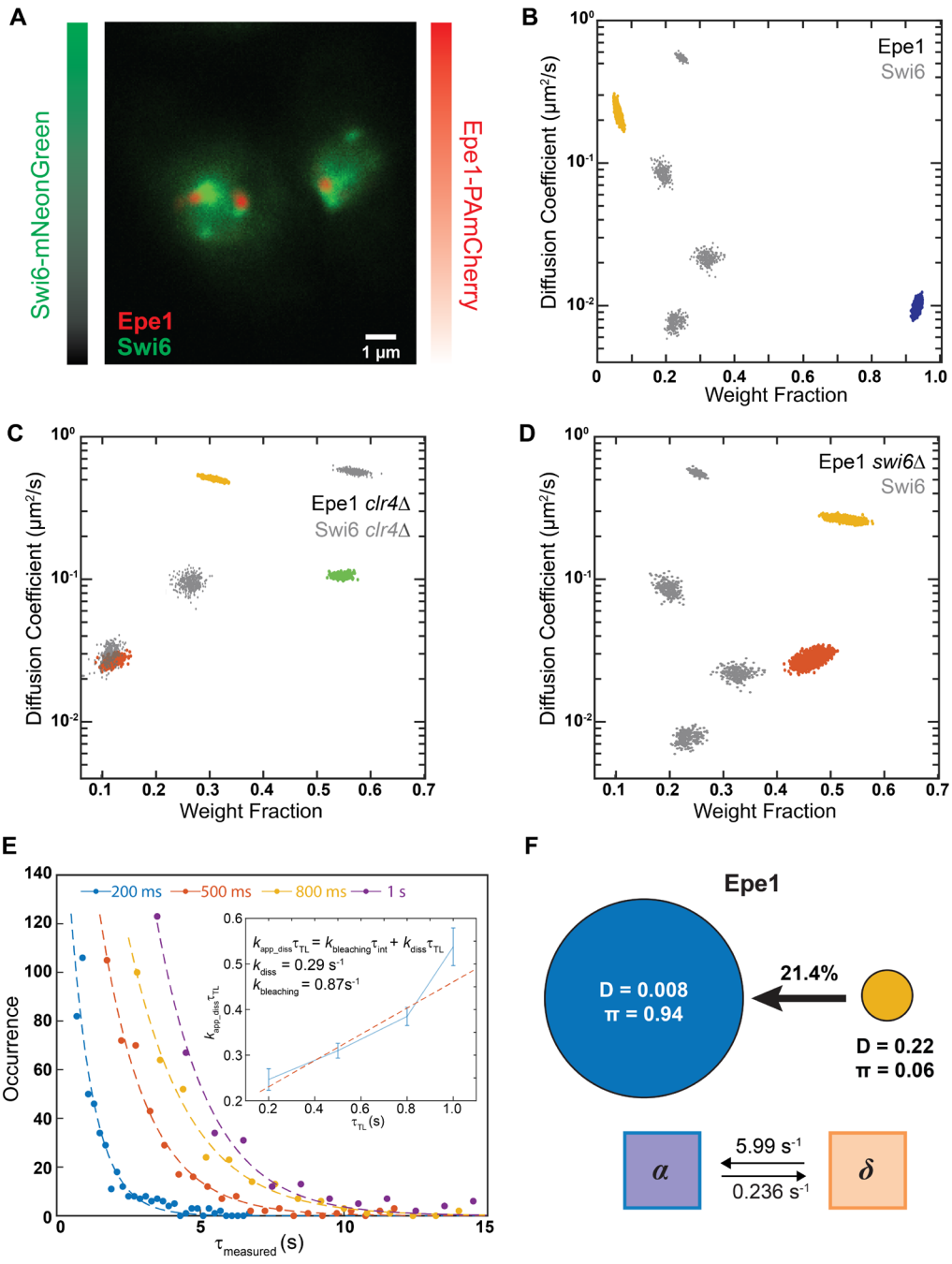

Figure 3. Single-molecule dynamics of Epe1 reveal that H3K9me reinforces the Swi6-Epe1 interaction on heterochromatin and suppresses off-site binding (caption on next page).

Figure 3. Single-molecule dynamics of Epe1 reveal that H3K9me reinforces the Swi6-Epe1 interaction on heterochromatin and suppresses off-site binding. A: Two-color imaging of cells expressing mNeongreen-Swi6 and Epe1-PAmCherry. Swi6 and Epe1 are expressed from their endogenous promoters. Green colorbar: Swi6-mNeonGreen intensities; Red colorbar: reconstructed Epe1-PAmCherry density map. Both color channels are normalized to the maximum pixel intensity. **B-D**: NOBIAS identifies distinct mobility states for Epe1-PAmCherry. Each colored point is the average single-molecule diffusion coefficient of PAmCherry-Chp2^{nmt81} molecules in that state sampled from the posterior distribution of NOBIAS inference at a saved iteration after convergence in WT cells (**B**), *clr4Δ* cells (**C**), and *swi6Δ* cells (**D**). Grey points are the previously reported PAmCherry-Swi6 single-molecule dynamics (24). **E**: Dwell time distributions for Epe1-PAmCherry expressed under its endogenous promoter. The distributions are shown with fits to an exponential decay. Insert: linear fit (red dashed line) of $k_{app\_diss}\tau_{TL}$ vs. τ_{TL}, from which the dissociation rate constant, k_{diss}, and the photobleaching rate constant $k_{bleaching}$ are obtained. Errors bars are from standard deviation of exponential decay fitting. **F:** Top: Transition probabilities between the two mobility states of Epe1-PAmCherry from **B**. Diffusion coefficients, *D*, in units of μm^2/s and weight fractions, π, are indicated. Bottom: Inferred rate constants for Epe1-PAmCherry from the fine-grained chemical kinetic simulation.

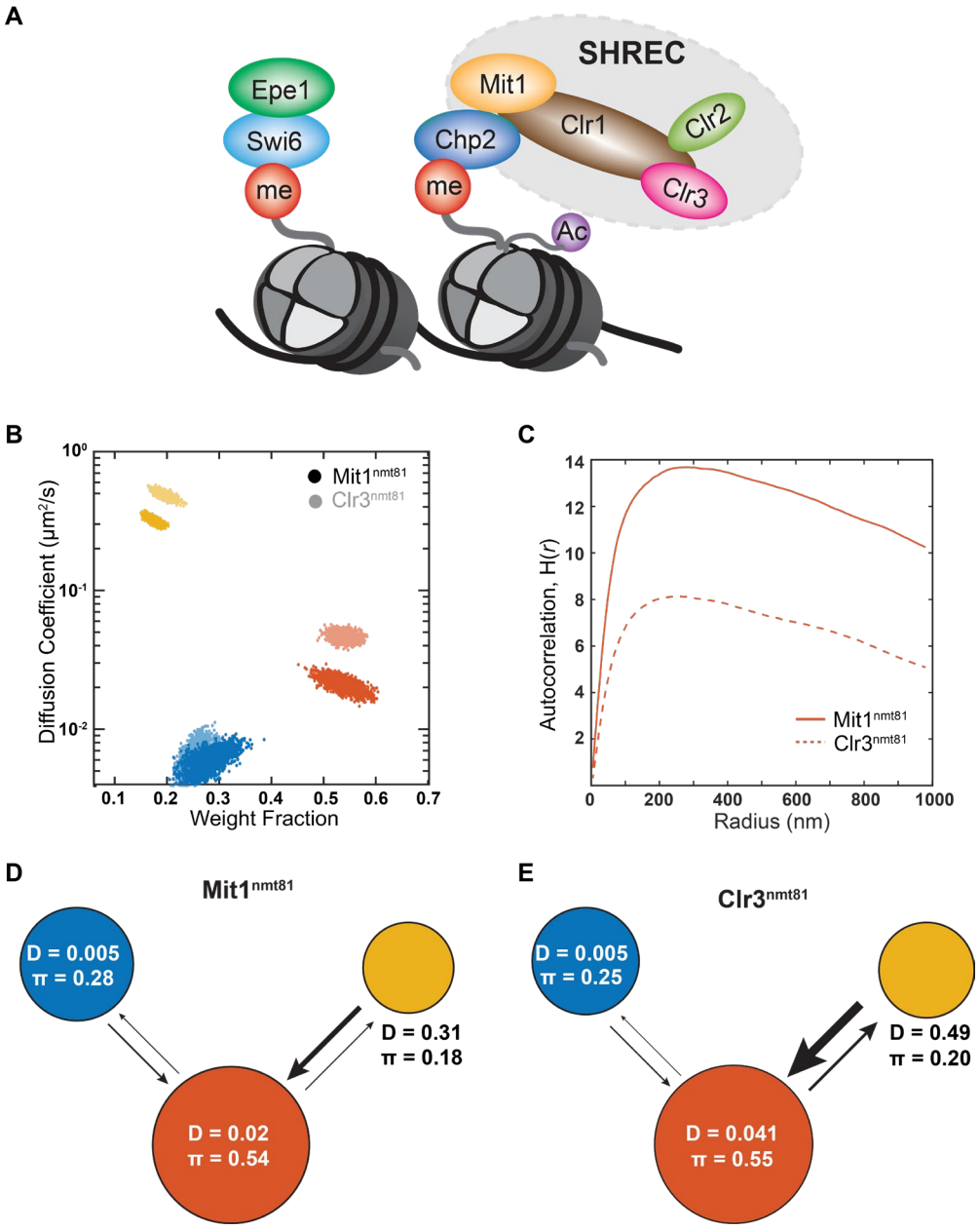

Figure 4. The two SHREC complex subunits proteins Mit1 and Clr3 only assemble at heterochromatin sites. A: Schematic of H3K9 methylated nucleosomes interacting with HP1 proteins and forming HP1 sub-complexes. Swi6 binds to Epe1; Chp2 interacts with the SHREC complex through Mit1. **B:** NOBIAS identifies three distinct mobility states for PAmCherry-Mit1^{nmt81} and PAmCherry-Clr3^{nmt81}. Each point is the average single-molecule diffusion coefficient of PAmCherry-Mit1^{nmt81} molecules (solid colored points) or PAmCherry-Clr3^{nmt81} molecules (transparent colored points) in that state sampled from the posterior distribution of NOBIAS inference at a saved iteration after convergence. **C:** The intermediate state of Mit1^{nmt81} (solid line) has a higher Ripley's H(r) than the intermediate state of Clr3^{nmt81} (dashed line). Each autocorrelation plot is normalized with randomly simulated trajectories from the same state (Methods). **D-E** Transition probabilities between the three mobility states of PAmCherry-Mit1^{nmt81} (**D**) and PAmCherry-Clr3^{nmt81} (**E**) from NOBIAS. The arrow widths are proportional to the transition probabilities. Diffusion coefficients, D, in units of μm^2/s and weight fractions, π, are indicated.

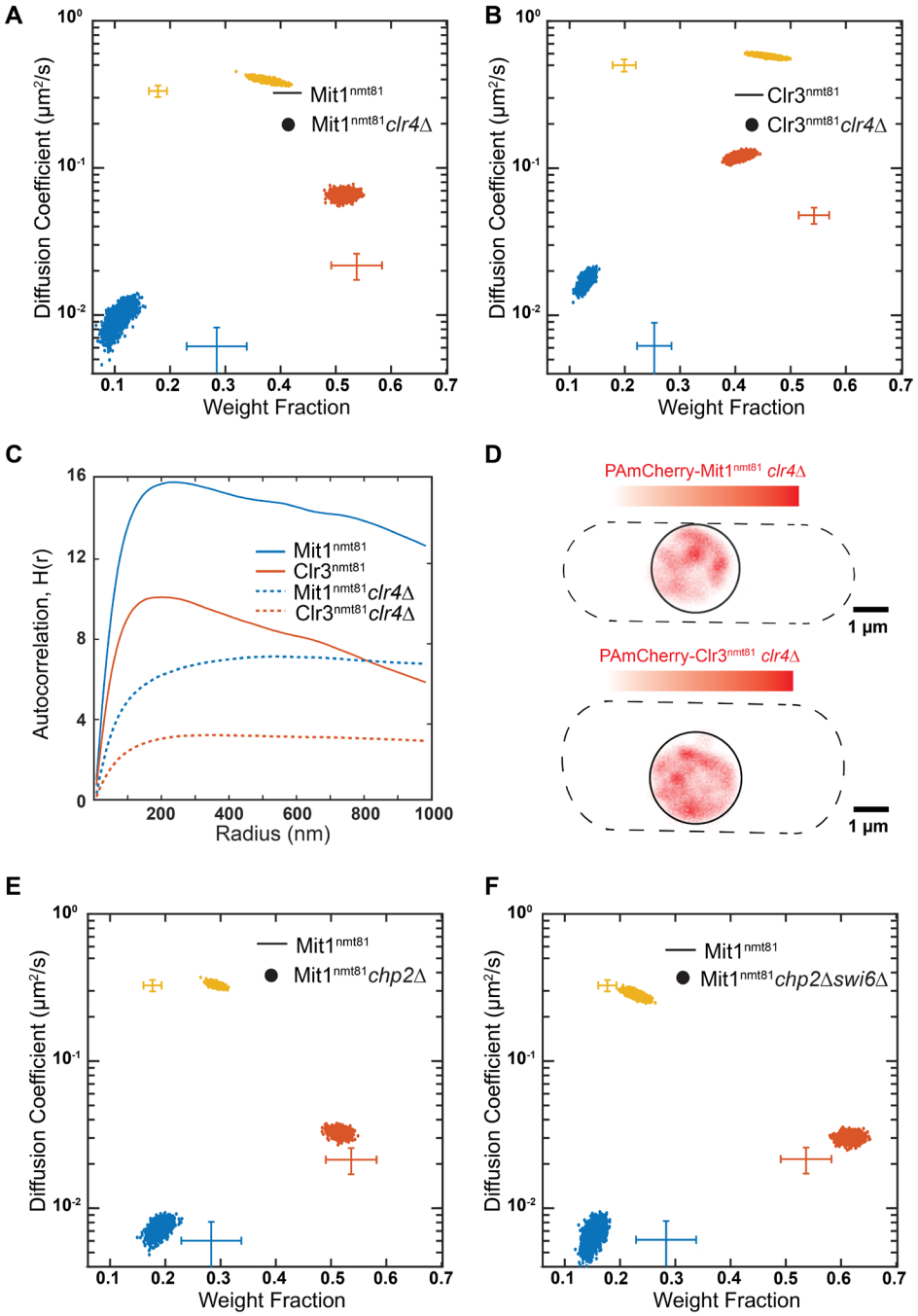

Figure 5. Chp2 associates with SHREC complex components only in the presence of H3K9 methylation. A-B: NOBIAS identifies three distinct mobility states for PAmCherry-Mit1^{nmt81} (**A**) and PAmCherry-Clr3^{nmt81} (**B**) in *clr4Δ* cells. Each colored point is the average single-molecule diffusion coefficient of molecules in that state sampled from the posterior distribution of NOBIAS inference at a saved iteration after convergence. The colored crosses show the data for PAmCherry-Mit1^{nmt81} and PAmCherry-Clr3^{nmt81} (Figure **4B**). **C:** Ripley's H analysis for steps from all states for Mit1^{nmt81} and Clr3^{nmt81} in WT cells and *clr4Δ* cells. Mit1^{nmt81} and Clr3^{nmt81} in *clr4Δ* cells have lower Ripley's H(*r*) values than Mit1^{nmt81} and Clr3^{nmt81} in WT cells. **D**: Reconstructed single-molecule density map for PAmCherry-Mit1^{nmt81} (top) and PAmCherry-Clr3^{nmt81} (bottom) in *clr4Δ* cells. Dashed lines: approximate *S. pombe* cell outlines; solid circles: approximate nucleus borders. **E-F**: NOBIAS identifies three distinct mobility states for PAmCherry-Mit1^{nmt81} in *chp2Δ* cells (**E**) and *chp2Δ swi6Δ* cells (**F**). Each colored point is the average single-molecule diffusion coefficient of molecules in that state sampled from the posterior distribution of NOBIAS inference at a saved iteration after convergence. The colored crosses show the data for PAmCherry-Mit1^{nmt81} in WT cells (Figure **4B**).

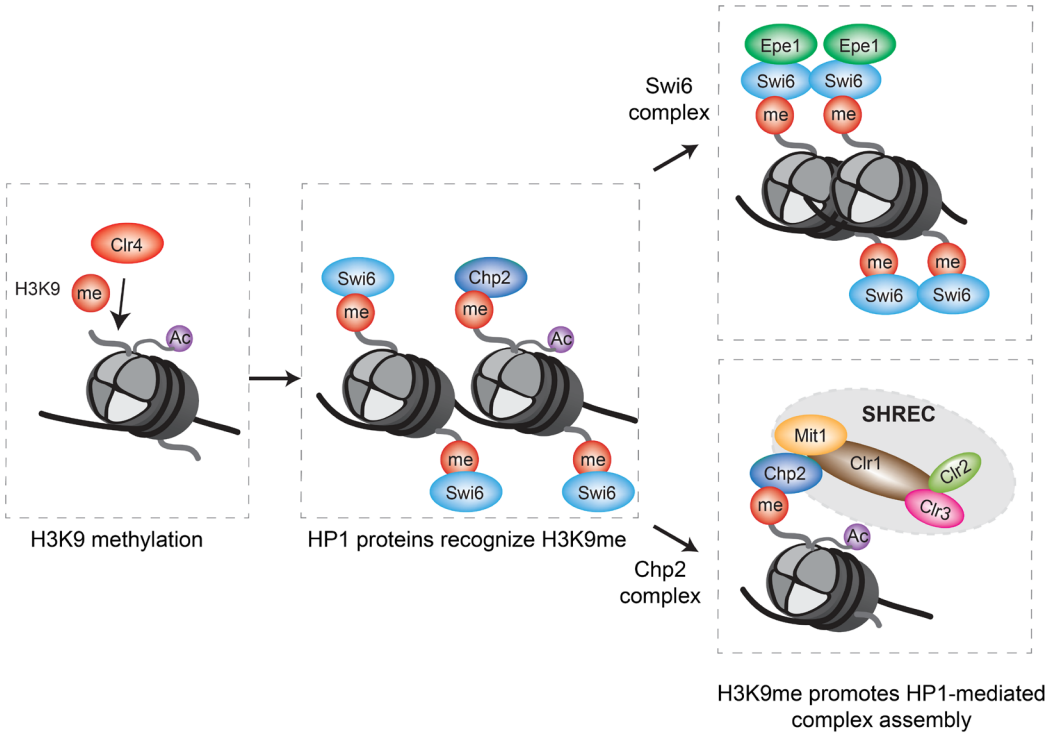

Figure 6. H3K9me enhances the assembly of HP1 protein complexes on chromatin sites. Left to right: The sequence-specific recruitment of Clr4 promotes H3K9 methylation deposition at sites of heterochromatin; HP1 proteins Swi6 and Chp2 recognize H3K9me with millisecond scale kinetics; H3K9me enhances Swi6 and Chp2 dependent protein complex assembly at sites of heterochromatin. The increased likelihood of complex formation at sites of H3K9me attenuates other possible off-chromatin interactions in the case of the Swi6 and Chp2 binding partners (Epe1, Mit1, and Clr3).